J. Fluid Mech. (2023), *vol*. 0, A1, doi:10.1017/jfm.2023.268

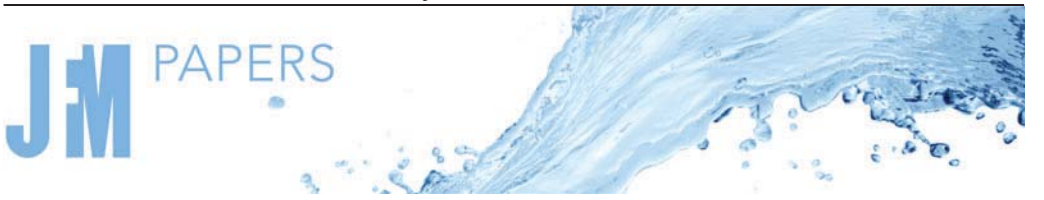

Vortex-induced vibration forever even with high structural damping

Peng Han[1], **Emmanuel de Langre**[2], **Mark C. Thompson**[3], **Kerry Hourigan**[3] **and Jisheng Zhao**[3,4,†]

[1]AML, Department of Engineering Mechanics, Tsinghua University, Beijing 100084, P. R. China

[2]LadHyX, CNRS, Ecole Polytechnique, Institut Polytechnique de Paris, 91128 Palaiseau, France

[3]Fluids Laboratory for Aeronautical and Industrial Research (FLAIR), Department of Mechanical and Aerospace Engineering, Monash University, Victoria 3800, Australia

[4]School of Engineering and Information Technology, University of New South Wales, Canberra, ACT 2600, Australia

(Received 20 September 2022; revised 4 March 2023; accepted 27 March 2023)

This study investigates the effect of structural damping on vortex-induced vibration (VIV) of a circular cylinder when the mass ratio is below its critical value. It is confirmed by water-channel experiments and a reduced-order model (ROM) that the previously identified phenomenon of VIV forever, i.e. resonance oscillations at any reduced velocity, persists even with high structural damping. Of interest, the ROM results reveal that the wake mode for VIV forever is unstable with a constant positive growth rate with increasing reduced velocity, while the experimental results suggest that VIV forever is associated with a synchronisation between the non-stationary cylinder vibration frequency and the vortex-shedding frequency.

Key words: flow-structure interactions, vortex instability, vortex shedding

1. Introduction

When an elastic or elastically mounted bluff body is subjected to a fluid flow, it may react to the vortex shedding and experience a phenomenon typical of fluid–structure interaction: vortex-induced vibration (VIV). One of the most profound characteristics of VIV is synchronisation (or 'lock-in'), where both the vortex shedding frequency and the body vibration frequency are locked and close to the natural frequency of the fluid–structure system (Williamson & Govardhan 2004; Païdoussis, Price & De Langre 2010). Generally, for cross-flow VIV of a circular cylinder with low mass and damping, the lock-in phenomenon occurs over a discrete finite range of reduced velocity. The lock-in

† Email address for correspondence: jisheng.zhao@unsw.edu.au

starts from the beginning of an upper branch, when the vortex-shedding frequency locks onto the body vibration frequency of the system in quiescent fluid, and extends through a lower branch, where the body vibration as well as the locked frequencies remain consistent. For a cylinder with a mass ratio above some value, desynchronisation may eventually occur at higher reduced velocity (e.g. Khalak & Williamson 1996; Williamson & Govardhan 2004). The reduced velocity is defined by $U_r = U/(f_{nw}D)$, where U is the free-stream velocity, D is the cylinder diameter and f_{nw} is the natural frequency of the system in quiescent fluid. It has been well established that the mass ratio (denoted by m^*, as the ratio of the total oscillating mass to the mass displaced by fluid) is an important parameter affecting the lock-in region as well as the body vibration amplitude response (Williamson & Govardhan 2004; Han & de Langre 2022). In a sequence of experiments, Govardhan & Williamson (2000) predicted and confirmed the existence of a critical mass ratio $m_c^* = 0.54$, below which resonant large-amplitude oscillations occurred at an infinite U_r for the Reynolds number range $4000 < Re < 22\,000$, where $Re = UD/\nu$, with ν being the kinematic viscosity of the fluid. This situation is referred to as 'VIV resonance forever' or briefly 'VIV forever'. It should especially be noted that, in the experiments of Govardhan & Williamson (2002), infinite reduced velocity (U_r^∞) is achieved by removing the physical restoring springs to realise $f_{nw} = 0$ and thus $U_r = \infty$. In the present study, we follow this concept first introduced by Govardhan & Williamson (2002) to perform VIV experiments at infinite reduced velocity.

Moreover, it has been demonstrated by both experimental and numerical studies that the critical mass ratio for VIV forever is dependent on the Reynolds number. For example, a critical mass ratio of $m_c^* = 0.25$ was found in a numerical study at $Re = 100$ of Shiels, Leonard & Roshko (2001). Later, Ryan, Thompson & Hourigan (2005) showed the existence of m_c^* in two low-Re regions in numerical simulations: the value of m_c^* decreased from approximately 0.5 to 0.1 for $40 \leq Re \leq 95$, and it remained approximately at 0.1 for $180 \leq Re \leq 200$, while no critical mass ratio was observed for the Re range in between these two regions. In their experimental study, Morse & Williamson (2009) reported that m_c^* increased with Re in the range from 4000 to 16 000, and then remained almost constant at $m_c^* = 0.54$ for $16\,000 < Re < 30000$. Recently, Navrose & Mittal (2017) investigated the effect of Reynolds number on the value of critical mass ratio. They confirmed the decreasing trend of m_c^* with Re increasing from 40 to 95 as reported by Ryan *et al.* (2005), and also showed that m_c^* increased from approximately 0.1 to 0.3 as Re was increased from 1000 to 4000, in line with the trend seen in the high-Re regime in the experiments of Morse & Williamson (2009).

On the other hand, the structural damping ratio is another parameter as important as the mass ratio and Reynolds number that can affect the characteristics of VIV such as the body vibration amplitude response and lock-in region. Generally, increasing the damping will reduce and even suppress the body vibration and the VIV lock-in region, as demonstrated by Blevins & Coughran (2009), Soti *et al.* (2018) and Zhao, Thompson & Hourigan (2022*a*). Research on the effect of structural damping on VIV is of great interest due to its implied influence on energy harvesting from VIV (see Soti *et al.* 2018; Zhao *et al.* 2022*a*).

Therefore, the following important open questions remain: (i) Will VIV be suppressed by high structural damping for a cylinder with a mass ratio below the critical value? (ii) Will the phenomenon of VIV forever disappear at high damping ratio? And, importantly, (iii) what is the mechanism underlying the phenomenon of VIV forever? Thus, in this study, by combining experiments and reduced-order modelling (ROM) in both nonlinear

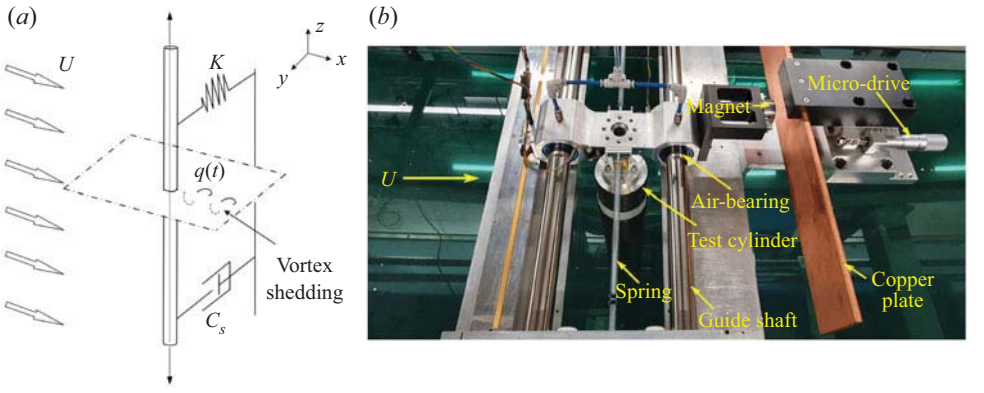

Figure 1. (*a*) A schematic of the problem studied, with the key parameters illustrated: free-stream velocity U, structural damping factor c_s, spring constant k and wake oscillator variable $q(t)$. (*b*) A photograph of the experimental set-up.

and linear forms, we aim to provide answers to the above questions. Indeed, VIV forever does persist even with high structural damping.

2. Methodologies

2.1. *Experimental details*

The flow–structure system was modelled based on a low-friction air-bearing rig in conjunction with a free-surface recirculating water channel of the Fluids Laboratory for Aeronautical and Industrial Research (FLAIR) at Monash University. Figure 1 shows a schematic of VIV of a circular cylinder and a photograph of the experimental set-up.

The test cylinder used was made from a lightweight and rigid carbon fibre tube, and it was precision manufactured using a grinding machine to have an outer diameter of $D = 71.34 \pm 0.01$ mm. The immersed length of the cylinder was $L = 614$ mm. The total oscillating mass was $m_s = 1003.8$ g, and the displaced fluid mass by the cylinder was $m_d = 2450.3$ g, giving a mass ratio of $m^* = m_s/m_d = 0.41$. In addition, for a better understanding of VIV below the critical mass ratio ($m_c^* \approx 0.54$), additional three mass ratios, $m^* = 0.50$ (close to the critical value), 6.07 and 25 (well above the critical value), were also included for comparison. An eddy-current-based damping mechanism was employed to control the structural damping by adjusting the gap between a magnetic element and a copper plate via a micro-drive stage with a resolution of 0.01 mm (see figure 1*b*). More details of this damper device can be found in the article of Soti *et al.* (2018). The structural damping ratio used in the present work is given by $\zeta = c_s/(2\sqrt{k(m_s + m_a)}) = \zeta_a f_{nw}/f_{na}$, where m_a is the (potential-flow) added mass given by $m_a = (f_{na}^2/f_{nw}^2 - 1)m_s$, $\zeta_a \cong c_s/(2\sqrt{km_s})$ is the damping ratio measured from free-decay tests in air and $f_{na} = 0.377 \pm 0.01$ Hz and $f_{nw} = 0.197 \pm 0.01$ Hz are the natural frequencies measured in quiescent air and water, respectively. Accordingly, an added mass coefficient was given by $C_M = m^*(f_{na}^2/f_{nw}^2 - 1) \approx 1.05$ from the free-decay tests. The topic of added mass has been discussed by Lighthill (1986), Govardhan & Williamson (2000), Limacher (2021) and Zhao, Thompson & Hourigan (2022*b*).

In the present cases of $m^* = 0.41$ with extension springs used, the VIV response was examined over a reduced velocity range of $3.0 \leq U_r \leq 15$; beyond this, an infinite U_r was tested in the absence of springs. The turbulence level of the free stream was less than 1 %. The corresponding Reynolds number range was $2870 \leq Re \leq 14\,330$, with an uncertainty

of ± 10. The cylinder displacement was measured using a non-contact digital optical linear encoder (model RGH24; Renishaw, UK) that had a resolution of 1 μm. For each reduced velocity, the measurement data were acquired at a sampling rate of 100 Hz for 300 s. More details of the experimental facility used can be found in the studies of Soti *et al.* (2018), Zhao, Hourigan & Thompson (2018) and Zhao *et al.* (2022*a*).

2.2. *Reduced-order modelling*

2.2.1. *Model description*

Along with the experiments, a numerical reduced-order model proposed by Facchinetti, de Langre & Biolley (2004) was also adopted to investigate the VIV problem. As shown in figure 1(*a*), the dynamics of a circular cylinder undergoing cross-flow VIV is considered simply as that of a linear oscillator governed by

$$m\ddot{Y} + (c_s + c_f)\dot{Y} + kY = F_v, \quad m = m_s + m_a, \tag{2.1}$$

where Y is the cylinder displacement, with the overdots representing time derivatives; and m_a, c_s and k represent the added mass, structural damping and stiffness, respectively. The added mass m_a is given by $m_a = C_M \rho D^2 \pi/4$, where ρ is the fluid density and $C_M = 1.05$ is obtained for the present experiments. It should be noted that the measurement of C_A is 5 % above the theoretical value $C_A = 1$ (in potential flow), which has a negligible effect on both the experimental and ROM results. (The previous study of Zhao *et al.* (2022*b*) also showed that a C_A value with 8 % above the theoretical value had a negligible effect on the fluid force decomposition for inline VIV of a circular cylinder.)

In the second term of (2.1), c_f represents the fluid-added damping, and it is given by $c_f = C_D/(2\rho UD)$ to describe the fluid loading, where C_D represents the 'amplified drag coefficient' (Facchinetti *et al.* 2004), noting that, herein, C_D is not the traditional drag coefficient (e.g. for flow past a fixed cylinder). The effect of fluid damping has been demonstrated in the recent study of Konstantinidis *et al.* (2020) showing that the drag acting in the direction opposite to the instantaneous relative velocity between the free-stream flow and the moving cylinder can induce a pure damping force (one that is 180° out of phase with respect to the cylinder movement velocity). In fact, the amplified drag coefficient C_D is a (nonlinear) function of the vibration characteristics and the traditional drag coefficient of flow over a fixed cylinder C_{D0}. However, for the sake of simplicity, it is often assumed to be constant (Facchinetti *et al.* 2004), typically $C_D \approx 2.0$ (e.g. Facchinetti *et al.* 2004; Violette, de Langre & Szydlowski 2007; Grouthier *et al.* 2013). In the present study, C_D was set to be constant at 1.9. The forcing term in (2.1), namely the transverse lift due to the unsteady vortex shedding F_v, can be obtained by

$$F_v = \rho U^2 D C_L^v/2 = \rho U^2 D q C_{L0}/4, \tag{2.2}$$

where C_L^v represents the unsteady vortex-induced lift coefficient of a vibrating cylinder, while C_{L0} represents the magnitude of lift coefficient of the fixed cylinder and the parameter $q/2$, as the ratio of C_L^v to C_{L0}, can be interpreted as a reduced vortex (or 'fluctuating') lift coefficient. A van der Pol nonlinear wake oscillator equation is introduced here to model the dimensionless wake variable q, coupled to the displacement Y

$$\ddot{q} + \varepsilon\omega_f(q^2 - 1)\dot{q} + \omega_f^2 q = (A/D)\ddot{Y}, \tag{2.3}$$

where ω_f is the vortex-shedding angular frequency defined as $\omega_f = 2\pi StU/D$, with St being the Strouhal number for flow over a stationary cylinder. In (2.3), $\varepsilon = 0.3$ and $A = 12$ are constant coefficients derived from experimental correlations

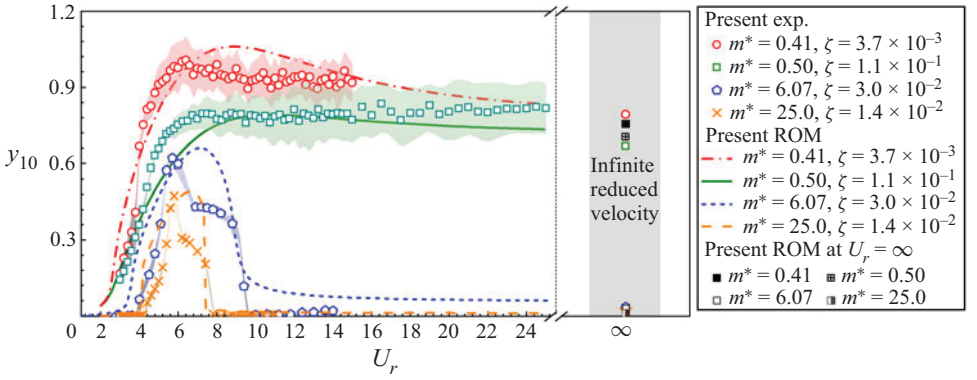

Figure 2. A comparison of the dimensionless amplitude response y_{10} as a function of reduced velocity U_r between the present experiments and ROM, with four mass ratios: $m^* = 0.41$ (well below m_c^*), 0.50 (close to m_c^*), as well as 6.07 and 25 (well above m_c^*). Note that the shaded areas represent the standard deviations of the experimental measurements of y_{10}.

(see Facchinetti *et al.* 2004; de Langre 2006). We now introduce the dimensionless drag-related parameter γ, time t, amplitude y, mass ratio m^*, structural angular frequency ω_s and damping ratio ζ, as follows:

$$\gamma = \frac{C_D}{4\pi St}, \quad t = T\omega_s, \quad y = Y/D, \quad m^* = \frac{4m_s}{\pi\rho D^2}, \quad \omega_s = \sqrt{k/m},$$
$$\zeta = \frac{c_s}{2\sqrt{km}} = \frac{c_s}{2m\omega_s}. \tag{2.4}$$

Substituting the dimensionless parameters into (2.1)–(2.3) yields coupled equations governing the displacement $y(t)$ and the wake variable $q(t)$

$$\ddot{y} + \left(2\zeta + \frac{4\gamma U_r St}{\pi m^* + \pi C_M}\right)\dot{y} + y = \frac{U_r^2 C_{L0}}{4\pi^3(m^* + C_M)} \cdot q, \tag{2.5}$$
$$\ddot{q} + \varepsilon U_r St(q^2 - 1)\dot{q} + (U_r St)^2 q = A\ddot{y}. \tag{2.6}$$

2.2.2. *Validation*

Numerically solving (2.5) and (2.6) with a second-order finite difference scheme in time subject to an initial perturbation to the cylinder displacement results in a limit cycle of $y(t)$ and $q(t)$. The simplicity of this set of equations allows modelling of the dynamics for an extremely low computational cost, yet well reproducing the effect of varying parameter values on the system response (see Facchinetti *et al.* 2004; de Langre 2006; Grouthier *et al.* 2013; Han & de Langre 2022). An additional validation is presented here as the ROM is applied to VIV for mass ratios below and well above the critical value. Figure 2 shows the dimensionless amplitude response, y_{10}, for different mass ratios obtained from the present experiments and the ROM. Note that y_{10} represents the mean of the top 10 % of the highest vibration amplitudes at each U_r. The model parameters for the ROM were set the same as for the experiments, except values for $St \approx 0.2$ and $C_{L0} \approx \sqrt{2}/2$ for flow over a fixed cylinder taken from Norberg (2003) in the same Re range as the present experiments. As can be seen in figure 2, the ROM results agree qualitatively and semi-quantitatively with the experiments, even though the mass ratio $m^* = 0.41$ is well below the critical value ($m_c^* \approx 0.54$). Additional comparisons with $m^* = 0.50$, 6.07 and 25 are also included in

figure 2, showing that the ROM can capture the approximate VIV magnitude and the extent of the resonant region for cases from close to m_c^* to well above m_c^*.

Moreover, at an infinite reduced velocity U_r^∞ (i.e. by removing the restoring springs in experiments or by setting zero spring stiffness in the ROM), both experiments and ROM show substantially large vibration amplitudes for $m^* = 0.41$ in figure 2, confirming that the occurrence of VIV forever in the present study, and that the ROM is an effective tool to investigate the problem of VIV forever.

We acknowledge that there are some discrepancies between the ROM predictions and experimental results, particularly in its failure to predict the lower branch for cases well above the critical mass ratio. This is mainly because the form of the proposed ROM, which is coupled only with the body acceleration $\ddot{y}$ (see the right-hand term in (2.6)), cannot capture the classical upper–lower-branch transition in VIV (Facchinetti *et al.* 2004). Possibly, introducing an out-of-phase term (i.e. the velocity $\dot{y}$) coupled together with the acceleration (Han *et al.* 2021), or adding a frequency-dependent term (e.g. Ogink & Metrikine 2010) may improve the accuracy of ROM; however, this would make the ROM implementation become more complicated, noting that the focus of this study is modelling of the effect of structural damping on VIV forever. The discrepancies between the ROM and experimental results may also be improved by optimising the input coefficients used in our ROM. For instance, the lift coefficient C_{L0} and the Strouhal number St of flow over a stationary cylinder in (2.5) and (2.6) have been found to scatter over certain Reynolds number ranges, depending on the authors (see Moeller 1982; Szepessy & Bearman 1992; Norberg 2003). A sensitive analysis of the parameters C_{L0} and St on ROM has been reported recently by Han & de Langre (2022). However, note that a different set of input coefficients for ROM will not change the mechanisms for the VIV phenomenon. In summary, through comparisons with the present experiments, the low-cost simplified ROM can qualitatively and to some extent quantitatively predict VIV and importantly the VIV forever phenomenon, despite its failure to capture the VIV upper–lower-branch transition.

2.3. *Linear stability analysis of the reduced-order model*

On the basis of a nonlinear ROM, de Langre (2006) developed a simplified linear stability analysis (LSA), which was successfully applied to predict the phenomenon of VIV forever for an undamped system (i.e. with zero damping). Inspired by this, we performed a similar LSA of the ROM (ROM-LSA) but including the structural damping to address the questions raised in § 1. In this ROM-LSA, eliminating all nonlinear terms in (2.5) and (2.6) gives

$$\ddot{y} + \left(2\zeta + \frac{4\gamma U_r St}{\pi m^* + \pi C_M}\right)\dot{y} + y = \frac{U_r^2 C_{L0}}{4\pi^3 (m^* + C_M)} \cdot q, \tag{2.7}$$

$$\ddot{q} - \varepsilon U_r St \dot{q} + (U_r St)^2 q = A\ddot{y}. \tag{2.8}$$

Further, assuming exponential time dependence $(y, q) = (y_0\, \mathrm{e}^{\lambda t}, q_0\, \mathrm{e}^{\lambda t})$ yields the frequency equation for the roots λ

$$D(\lambda; R) = \lambda^4 + (R - \varepsilon U_r St)\lambda^3 + (U_r^2 St^2 - AHU_r St - \varepsilon U_r StR + 1)\lambda^2 + (U_r^2 St^2 R - \varepsilon U_r St)\lambda + U_r^2 St^2, \tag{2.9}$$

$$R = 2\zeta + \frac{4\gamma U_r St}{\pi m^* + \pi C_M}, \quad H = \frac{C_{L0}}{4\pi^3 St^2 (m^* + C_M)}. \tag{2.10a,b}$$

Expanding the root λ about its undamped value to include the influence of damping represented by R, we can obtain $\lambda = \lambda_0 + R\lambda_R$. Here, λ_0 satisfies the frequency equation without the damping parameter R, i.e. $D(\lambda_0; 0) = 0$. Similarly, expanding (2.9) gives

$$D(\lambda_0 + R\lambda_R; R) = D(\lambda_0; 0) + R\lambda_R \left.\frac{\partial D}{\partial \lambda}\right|_{(\lambda_0;0)} + R \left.\frac{\partial D}{\partial R}\right|_{(\lambda_0;0)} = 0. \tag{2.11}$$

After some elementary algebra, the effect of structural damping ratio ζ on the root λ can be obtained resulting in the following expression:

$$\lambda = \lambda_0 - R\frac{\partial D/\partial R}{\partial D/\partial \lambda} = \lambda_0 - \left(2\zeta + \frac{4\gamma U_r St}{\pi m^* + \pi C_M}\right) \frac{\lambda_0^4 - \varepsilon U_r St \lambda_0^3 + (U_r St)^2 \lambda_0^2}{2\lambda_0^4 - 3\varepsilon U_r St \lambda_0^3 - 2(U_r St)^2 - \varepsilon U_r St \lambda_0}. \tag{2.12}$$

Solving the above equations gives the solution for λ, noting that its imaginary part, denoted by λ_i, is the angular frequency, while the ratio of its real part to its imaginary part yields the normalised growth rate, namely $G = \lambda_r/\lambda_i$. It should also be noted that there are two pairs of conjugate solutions, of which only the root with a positive imaginary part is of interest.

Following Han & de Langre (2022), for a given root, the ratio of the structural vibration amplitude y_0 to the magnitude of the wake variable q_0 can be obtained from (2.7) and (2.8)

$$\frac{y_0}{q_0} = \frac{\lambda^2 - \lambda\varepsilon U_r St + U_r^2 St^2}{\lambda^2 A} = \frac{U_r^2 C_{L0}}{4\pi^3 (m^* + C_M)\left(\lambda^2 + \lambda\left[2\zeta + \dfrac{4\gamma U_r St}{\pi(m^* + C_M)}\right] + 1\right)}. \tag{2.13}$$

By setting the numerator equal to zero, i.e. $q_0 \gg y_0$, we can derive the root for the case where the cylinder is fixed ($y \equiv 0$), corresponding to a pure wake mode (PW)

$$\lambda_{PW} = \frac{\varepsilon \pm \sqrt{\varepsilon^2 - 4}}{2} \cdot U_r St, \quad G_{PW} = \frac{\varepsilon}{\sqrt{4 - \varepsilon^2}}. \tag{2.14a,b}$$

The pure wake mode growth, G_{PW}, will be used to identify the mode in the roots obtained from (2.9) and (2.12), where the dynamics is mainly in the wake variable q. Conversely, the pure structural mode is defined by setting the denominator in (2.13) equal to zero. More specifically, via (2.12), when the solved growth rate G is close to the G_{PW}, it will be considered as a wake mode; on the other hand, if the mode shape is dominant in y, we label it as a solid mode (de Langre 2006; Violette, de Langre & Szydlowski 2010; Grouthier *et al.* 2013; Han & de Langre 2022). The ROM-LSA will give two modes – each can be stable or unstable with two degrees of freedom. For the wake mode, we define that it is unstable when the mode growth rate is higher than G_{PW}, while for the solid mode it is unstable when the mode growth rate is positive, following Han & de Langre (2022).

3. Results and discussion

3.1. *Effect of structural damping on VIV forever*

In the present study, the phenomenon of VIV forever indeed persists across a wide range of structural damping ratios. This can clearly be seen from the normalised amplitude y_{10} at $m^* = 0.41$ in figure 3. As shown in figure 3(*a*), the damping ratio range tested covers a wide range from 3.7×10^{-3} to 2.3×10^{-1}, with the highest value more than 62

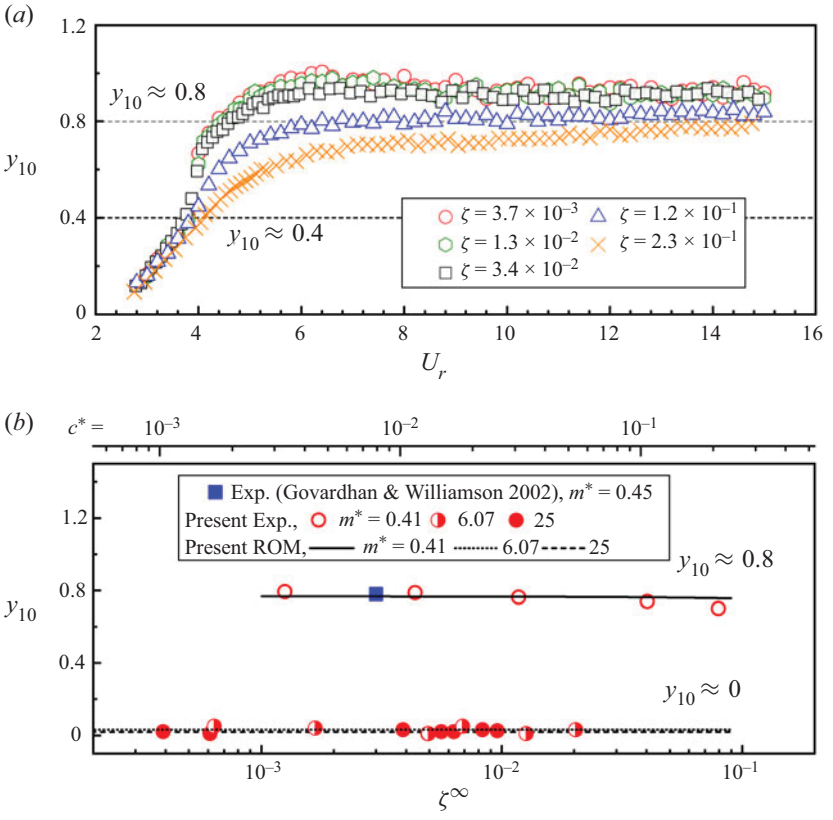

Figure 3. (*a*) The normalised amplitude response (y_{10}) as a function of reduced velocity (U_r) for various damping ratios at $m^* = 0.41$ in the present experiments. (*b*) The y_{10} response as a function of ζ^∞ at an infinite reduced velocity U_r^∞ of the present experiments in comparison with the present ROM and the experiments of Govardhan & Williamson (2002).

times of the lowest. Even with the highest damping ratio $\zeta = 2.3 \times 10^{-1}$, at which VIV suppression could result for a cylinder with a mass ratio above the critical value (e.g. Soti *et al.* (2018), $m^* = 3.0$), the cylinder can still oscillate with large amplitudes of $\sim O(1D)$ at high reduced or even infinite reduced velocities. Here, we define the ' large-amplitude' region as the region where, for a given damping ratio, y_{10} is higher than the half of the maximum value observed in the present study. It should be noted that for a cylinder with m^* above its critical value, e.g. $m^* = 3.0$ in Soti *et al.* (2018), and $m^* = 21.8$ in Blevins & Coughran (2009), VIV forever does not exist and the large-amplitude region tends to shrink with increasing ζ. It even leads to VIV suppression at a certain high damping ratio. Interestingly, the present result indicates that the effect of structural damping on VIV with a mass ratio under the critical value is distinctly different from the effect in those cases above the critical mass ratio.

To further confirm the above finding, we experimentally and numerically tested the vibration response at an infinite reduced velocity, by removing the restoring springs but keeping the same structural damping factor (c_s) settings as in figure 3(*a*). It should be noted that the structural damping ratio ζ is defined based on the natural frequency ω_s in (2.4); however, ζ will become infinite, when ω_s becomes zero in the absence of spring stiffness. To describe the damping effect in the absence of ω_s, we refer to the parameter

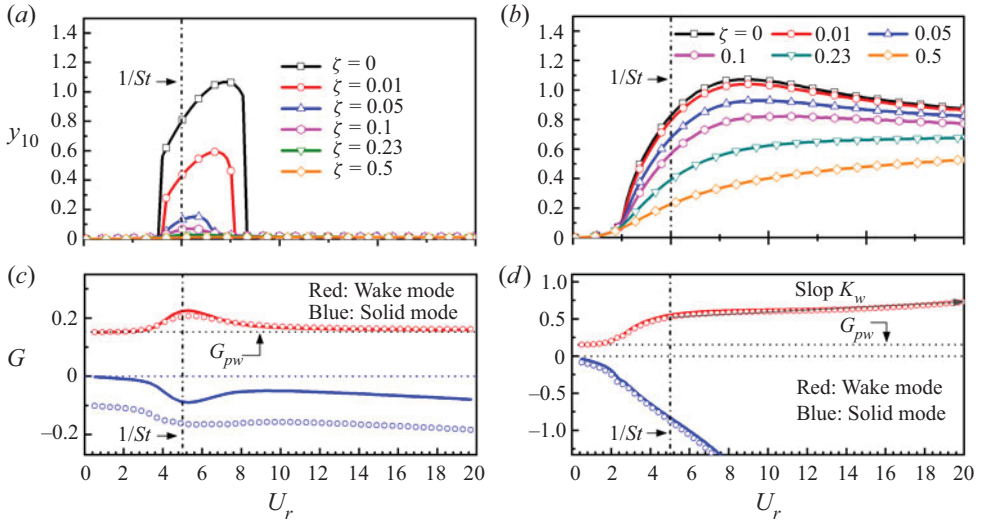

Figure 4. Effect of ζ on the y_{10} amplitude response for (*a*) $m^* = 25$ and (*b*) $m^* = 0.4$ obtained by ROM, together with the variations of growth rate G of the modes obtained by ROM-LSA, as a function of U_r. Note that in (*c*) and (*d*) the solid lines denote the results for low damping ratios, while the open circles denote the results for high damping ratios.

$\zeta^\infty = c_s/(2m\omega_f)$, which is based on the angular vortex-shedding frequency (ω_f) of a stationary cylinder (see Govardhan & Williamson 2002). For the infinite reduced velocity tested at $Re = 13\ 500$ in the study, the resultant damping ratio range is $\zeta^\infty = 1.2 \times 10^{-3}$–$8.0 \times 10^{-2}$ corresponding to its finite counterpart $\zeta = 3.7 \times 10^{-3}$–$2.3 \times 10^{-1}$. For a VIV system in the absence of a 'natural' frequency (i.e. without restoring springs), one may consider using another dimensionless form of damping ratio that is based on the advective time scale: $c^* = c_s D/(mU)$ (see Leontini *et al.* 2018). In figure 3(*b*), the corresponding range of c^* is from 0.003 to 0.210.

As shown in figure 3(*b*), the phenomenon of VIV forever is confirmed by both the experimental and ROM results for $m^* = 0.41$, which are in excellent agreement, evidenced by the consistent amplitude responses of $y_{10} \simeq 0.8$ through the ζ^∞ range tested. The present results are also in excellent agreement with the experiments with $m^* = 0.45$ and $\zeta \approx 0$ by Govardhan & Williamson (2002). Additional cases are also included to compare with the experimental and ROM cases at $m^* = 6.07$ and 25 well above m_c^*, where negligible vibration is observed. Nevertheless, these results clearly show that VIV forever persists for an underdamped cylinder (i.e. $\zeta < 1$) despite high damping ratio values.

To gain a better understanding of the damping effect on the VIV response of a cylinder at $m^* = 0.4$ and 25, a full nonlinear ROM based on (2.5) and (2.6) is adopted to evaluate the y_{10} response for different damping ratios, while a ROM-LSA based on (2.9), (2.12) and (2.14*a*,*b*) is used to assess the normalised instability growth rate G. As shown in figure 4(*a*,*c*), the amplitude response for the case of $m^* = 25$ is consistent with previous studies, confirming that increasing ζ reduces the VIV response. As expected, at $U_r \approx 1/St \approx 5$, where VIV resonance generally occurs, the G values of the wake mode clearly depart from the horizontal line of G_{pw} that represents the pure wake mode for a fixed cylinder (see (2.14*a*,*b*)). This means that the wake mode becomes much more unstable than the pure wake G_{pw}. Note that the departure range of the wake mode growth rate from G_{PW} is found to be $4 \lesssim U_r \lesssim 9.5$, which is consistent with the ROM in figure 4(*a*)

and experiments in figure 2, where significant vibration occurs. Moreover, the growth rate of the solid mode is always negative, indicating that the cylinder vibration is induced only by the wake mode (see Han & de Langre 2022). On the other hand, for the case of $m^* = 0.4$, the growth rate is always much greater than that of the pure wake after $U_r \gtrsim 1$, and tends to increase with increasing reduced velocity. This means that obvious structural vibration starts at a low U_r value and it will persist in the tested U_r range, due to the consistent unstable wake mode. Again, the above ROM-LSA results are consistent with the ROM results in figure 4(*b*) and the experiments at $m^* = 0.41$ in figure 2. Thus, it can be concluded that the primary cause for VIV forever is the highly unstable wake mode. Note that G increases linearly with a positive slope K_W for $U_r > 1/St$, and this slope is found to be almost independent of ζ. This is distinctly different from the case of $m^* = 25$, where the unstable wake mode occurs over a limited resonance region around $U_r \approx 1/St$. Since the ROM-LSA is a linear approximation, the slope K_W may be used as a simple tool to assess the occurrence of VIV forever. However, it should be noted that the LSA itself cannot predict the limit cycle but, as has been shown, it can to some extent predict where and why limit cycles of oscillations occur.

The effect of damping ratio on VIV forever can be further explained by deriving a relation of the vibration amplitude at U_r^∞ from the nonlinear ROM. We assume that the fluid–structure system is governed by (2.5) and (2.6) and that the cylinder vibration and the wake variable are $y(t) = y_0 \cos(\omega t)$ and $q(t) = q_0 \cos(\omega t + \phi)$, respectively, where y_0 is the cylinder vibration amplitude, q_0 is the magnitude of the wake variable, ω is the dimensionless angular vibration frequency and ϕ is the relative phase angle between the driving fluid force and the body displacement. Substituting them into (2.5) (i.e. the structural oscillator) yields

$$y_0 - y_0\omega^2 - \frac{U_r^2 C_{L0}}{4\pi^3(m^* + C_M)} \cdot q_0 \cos\phi = 0, \tag{3.1}$$

$$\frac{U_r^2 C_{L0}}{4\pi^3(m^* + C_M)} \cdot q_0 \sin\phi - 2\omega y_0 \zeta - \frac{4\gamma\omega U_r St}{\pi(m^* + C_M)} y_0 = 0. \tag{3.2}$$

Hereby, we can obtain a relationship between $y(t)$ and $q(t)$

$$y_0 = \frac{U_r^2 C_{L0}/[4\pi^3(m^* + C_M)]}{\left((\omega^2 - 1)^2 + \left[2\zeta + \dfrac{4\gamma U_r St}{\pi(m^* + C_M)}\right]^2 \omega^2\right)^{0.5}} \cdot q_0. \tag{3.3}$$

Similarly, by substituting $y(t) = y_0 \cos(\omega t)$ and $q(t) = q_0 \cos(\omega t + \phi)$ into (2.6) (i.e. the wake oscillator), and considering only the main harmonic contribution in the nonlinear dynamics, we can obtain the following set of equations:

$$U_r^2 St^2 q_0 - \omega^2 q_0 + A\omega^2 y_0 \cos\phi = 0, \tag{3.4}$$

$$\varepsilon U_r St \omega q_0 (1 - \tfrac{1}{4} q_0^2) + A\omega^2 y_0 \sin\phi = 0. \tag{3.5}$$

Now, the magnitude of the wake variable can be computed by

$$q_0 = 2\left(1 + A\omega^2 \frac{\dfrac{U_r^2 C_{L0}}{4\pi^3(m^* + C_M)}\left[2\zeta + \dfrac{4\gamma U_r St}{\pi(m^* + C_M)}\right]}{\varepsilon U_r St\left((\omega^2 - 1)^2 + \left[2\zeta + \dfrac{4\gamma U_r St}{\pi(m^* + C_M)}\right]^2 \omega^2\right)}\right)^{0.5}. \tag{3.6}$$

In addition, the angular vibration frequency ω and reduced velocity U_r should satisfy

$$U_r^2 St^2 + A\omega^2 \frac{\dfrac{(1-\omega^2)U_r^2 C_{L0}}{4\pi^3(m^*+C_M)}}{(\omega^2-1)^2 + \left[2\zeta + \dfrac{4\gamma U_r St}{\pi(m^*+C_M)}\right]^2 \omega^2} - \omega^2 = 0. \tag{3.7}$$

Combining equations (3.3) and (3.6), after some elementary algebra, we can finally describe the vibration amplitude y_0 with the previously defined dimensionless parameters.

From an order-of-magnitude analysis on (3.7), we can find that ω goes to infinity at U_r^∞. Then, importantly, considering the structural damping ratio ζ is a finite value (particularly $0 \leq \zeta < 1$ for an underdamped system), the damping-related terms in (3.3) and (3.6) can therefore be simplified as follows:

$$\left[2\zeta + \frac{4\gamma U_r^\infty St}{\pi(m^*+C_M)}\right] \approx \frac{4\gamma U_r^\infty St}{\pi(m^*+C_M)} = \frac{C_D U_r^\infty}{\pi^2(m^*+C_M)}. \tag{3.8}$$

The above expression indicates that the structural damping ratio (underdamped) has a negligible effect on the body vibration amplitude at an infinity reduced velocity. This is in agreement with the experimental results in figure 3, where the vibration amplitudes appear to be almost constant at an infinite reduced velocity for the damping ratio range tested. The damping effects can also be examined by solving (3.3) and (3.6). For instance, by using the same parameters as in figure 4(*a*,*b*) and setting the reduced velocity to infinity, we obtain $y_0 \approx 0.66$ and 0.01 for $m^* = 0.4$ and 25, respectively, in the tested range of $0 \leq \zeta \leq 0.5$. These estimates of y_0 at U_r^∞ are consistent with the findings from experiments and the nonlinear ROM in figure 3(*b*), where y_{10} values appear to be independent of damping (ζ^∞) for m^* cases below or above m_c^*. Note that the presence of significant vibration at U_r^∞ is the criterion for determining the occurrence of VIV forever. In other words, (3.3) and (3.6) clearly indicate that for an underdamped system, the structural damping will have a negligible effect on the vibration amplitude in VIV forever, which is consistent with the results from both the present ROM-LSA and experiments.

By neglecting all damping terms in his ROM-LSA, de Langre (2006) derived the upper limit of lock-in for VIV of a circular cylinder

$$U_r^{max} = \left[St - \sqrt{\frac{AC_{L0}}{4\pi^3(m^*+C_M)}}\right]^{-1}. \tag{3.9}$$

By letting U_r^{max} go to infinity, de Langre (2006) further derived the critical mass ratio that allows infinite resonance

$$m_c^* = AC_{L0}/(4\pi^3 St^2) - C_M. \tag{3.10}$$

The above (3.10) indicates that the parameters C_{L0}, St, and C_M can affect m_c^*. Recently, in their numerical study of FIV of an elliptical section (of 1.5 in the cross-sectional aspect ratio) with $m^* = 1$ at $Re = 200$, Leontini *et al.* (2018) have shown that the critical mass is the mass which results in an inertial force that can be balanced by the magnitude of the lift force – in other words, m_c^* is set by the magnitude of the lift force. They have also demonstrated that the bluffer geometry of an ellipse (compared with a circular section) could potentially generate a larger magnitude of lift force, and thus should have a higher m_c^* value than the circular counterpart – they observed that the ellipse at a 90° angle of attack exhibited an infinite resonance at $m^* = 1$, a much higher value than the critical mass

ratio expected for the circular cylinder in that *Re* regime. The above results from Leontini *et al.* (2018) could potentially be extended to account for the damping resistance force in the sense that the effect of damping (ratio) would reduce the magnitude of lift force (as reflected by reduced body vibration), thus resulting in a lower m_c^* value; in other words, an increase in the structural damping would require a decrease in the cylinder mass (i.e. a lighter cylinder) to exhibit VIV forever. Thus, we hypothesise that the structural damping is another factor that can potentially affect the critical mass ratio. However, to test this hypothesis would require accurate measurements of the critical mass ratio values under various damping ratios (i.e. via a parametric study with fine increments in both mass and damping ratios), which is beyond the focus of the present study.

3.2. *Frequency analysis*

To provide insight into the dynamics of cylinder vibration in VIV forever, this subsection presents a frequency analysis of the cylinder vibration and fluid forcing in experiments.

Figure 5 shows the normalised logarithmic-scale power spectrum density (PSD) contours of the cylinder vibration frequency response for $m^* = 0.41$ with various damping ratios ($\zeta = 3.7 \times 10^{-3}$–$2.3 \times 10^{-1}$) from the present experiments and ROM. The construction method for this figure can be found in the previous studies of Leontini, Lo Jacono & Thompson (2011, 2013) and Zhao *et al.* (2014, 2018). As can be seen, the dominant frequencies (denoted by open circles) are in good agreement with the results of Govardhan & Williamson (2002) (denoted by solid diamonds); however, considerable broadband frequency components appear in the upper branch region (i.e. $U_r > 4$), which are distinctly different from those of the conventional upper branch with m^* well above critical value, where the cylinder vibration clearly displays a single frequency (e.g. Zhao *et al.* 2018). Overall, the body vibration frequency increases linearly with U_r after y_{10} becomes relatively stable (e.g. $U_r > 6$). The slope of the linear frequency variation is observed to increase slightly from $a = 0.148$ to 0.154 across a damping ratio increase of the order of 2 from $\zeta = 3.7 \times 10^{-3}$ to 2.3×10^{-1}. It can also be seen that in the upper-branch region, in all cases the body vibration frequency departs significantly from the Strouhal number trend (i.e. $St \simeq 0.215$ measured for the fixed cylinder), which is similar to the conventional upper-branch response with m^* of the order of $O(1)$ above m_c^*. On the other hand, the present ROM also quantitatively captures linear frequency-response variations with their slope values increasing from 0.114 to 0.128 across the damping ratios tested. Nevertheless, the above results imply that the large-amplitude vibration seen for sub-critical mass ratio (i.e. $m^* < m_c^*$) is strongly associated with a synchronisation between the cylinder vibration frequency and the vortex-shedding frequency, rather than the natural frequency (i.e. f_{nw}) of the system. Due to the coupled fluid–structure interaction, the vortex-shedding frequency from a vibrating body in synchronisation appears to be significantly lower than that of the fixed body counterpart, and the vortex-shedding frequency tends to increase as the body vibration is reduced by the damping effect; however, the fluid–structure (frequency) synchronisation remains strong for a sub-critical mass ratio within the underdamped damping ratio range (i.e. $\zeta < 1$).

To provide a further insight into frequency synchronisation, figure 6 shows a time–frequency analysis based on continuous wavelet transform (CWT) for the cylinder vibration and fluid forcing. Details of the CWT used can be found in Zhao *et al.* (2022*b*). For the upper branch ($U_r = 5.6$) of $m^* = 25$ shown in figure 6(*a*), the normalised vibration frequency (f_y^*) clearly locks onto the natural frequency of the system (f_{nw}), and remains stationary (not varying) over time, while the fluid forcing frequency ($f_{C_L}^*$) also

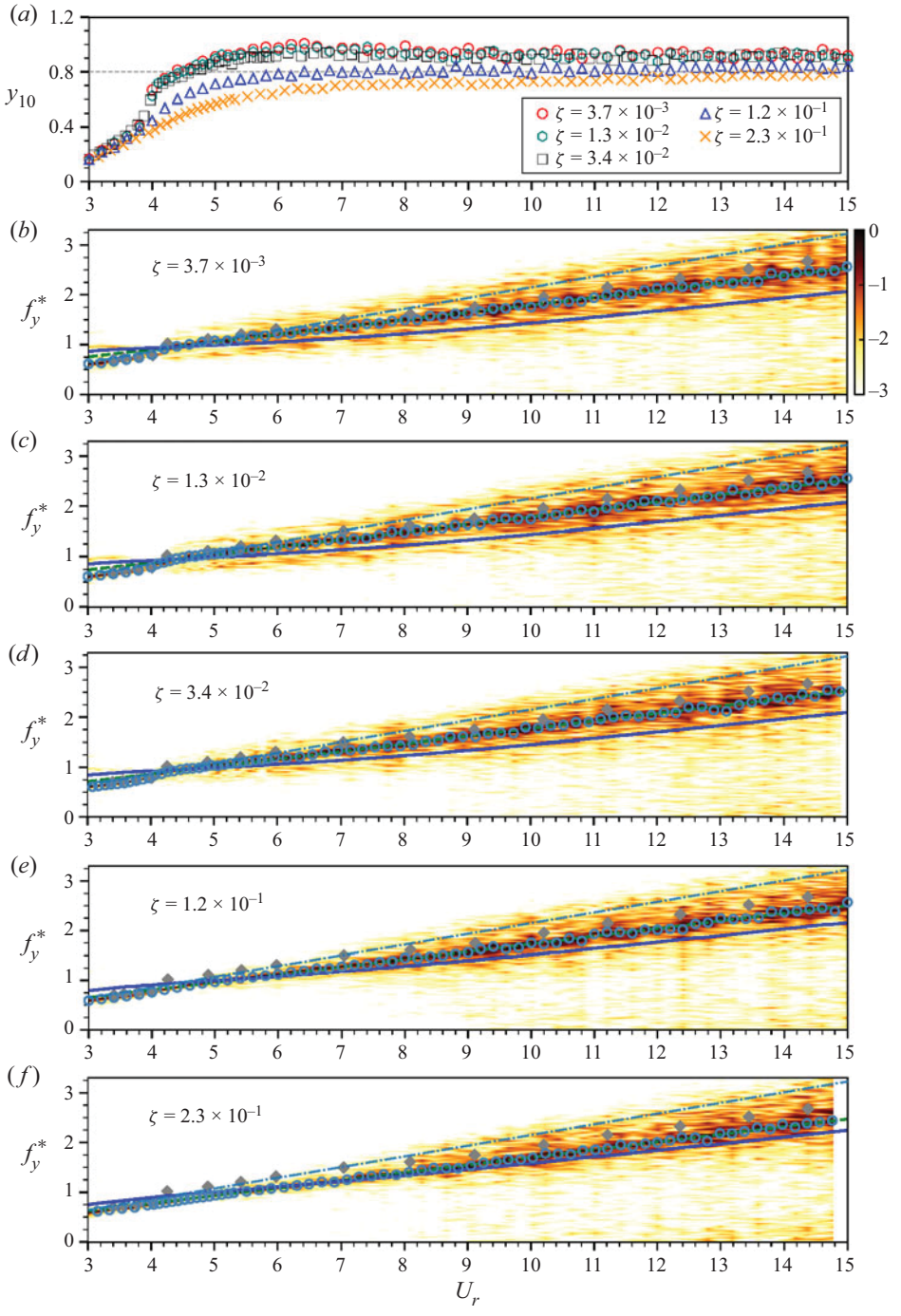

Figure 5. Logarithmic-scale power spectrum density contours of normalised frequency response as a function of reduced velocity for the present experiments of $m^* = 0.41$ with various damping ratios in (*b*) – (*f*). Note that (*a*) revisits their normalised amplitude responses. The cylinder vibration frequency is normalised by the natural frequency, namely $f_y^* = f_y/f_{nw}$. The open circles represent the local dominant frequency component in the present experiments, while the solid diamonds in (*b*) represent the measurements with $m^* = 0.52$ (ζ unknown) by Govardhan & Williamson (2002). The dashed-dotted lines represent the Strouhal number frequency ($St \simeq 0.215$), the dashed lines (green) represent the trend slope of the dominant frequency for $U_r \geq 6$, where y_{10} appears to be relatively stable with increasing U_r, and the solid lines (blue) represent the normalised frequency response obtained from the corresponding ROM.

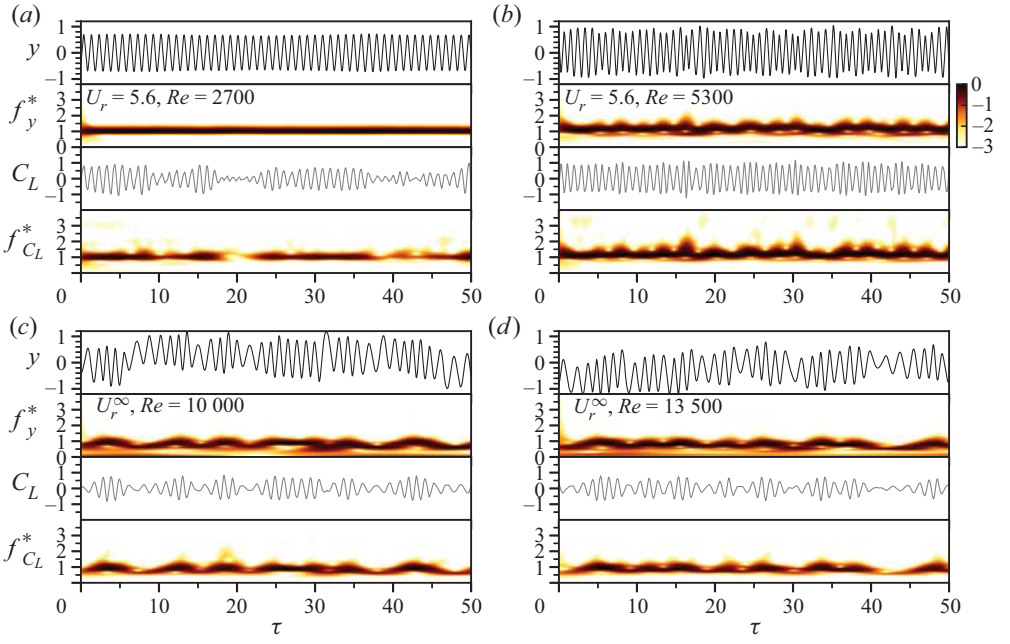

Figure 6. Continuous-wavelet-transform-based time–frequency analysis for the cylinder vibration and transverse lift force: the case of $m^* = 25$ and $\zeta = 8.55 \times 10^{-4}$ at $U_r = 5.6$ in (*a*); and the case of $m^* = 0.41$ and $\zeta = 3.70 \times 10^{-3}$ at $U_r = 5.6$ in (*b*), U_r^∞ and $Re = 10\,000$ in (*c*) and U_r^∞ and $Re = 13\,500$ in (*d*). Note that the frequency PSD contours are logarithmic scaled; in (*c*) and (*d*) the frequency components in the absence of springs are normalised by f_{vs}.

locks onto f_{nw} but exhibits noticeable discontinuities in power over time. On the other hand, for the case at $U_r = 5.6$ of $m^* = 0.41$, f_y^* is clearly synchronised with $f_{C_L}^*$, and interestingly they become non-stationary, varying around a value slightly above f_{nw} over time. Moreover, the non-stationary frequency synchronisation can also be seen in VIV forever at two different Reynolds numbers ($Re = 10\,000$ and $13\,500$) in figure 6(*c*,*d*). However, it should be noted that, without restoring springs, the equilibrium position of the cylinder vibration in VIV forever appears to the unstable. Perhaps this is unsurprising, since the magnitude of lift force generated by the vortex shedding is naturally unstable. Nevertheless, the irregular non-stationary behaviour of both f_y^* and $f_{C_L}^*$ for the $m^* = 0.41$ case may suggest a frequency synchronisation of chaos, where the cylinder vibration frequency is synchronised with the fluid forcing frequency but the dynamics appears to be chaotic.

4. Conclusions

Vortex-induced vibration of a circular cylinder with a low mass ratio below the critical value has been investigated over a wide range of structural damping in water-channel experiments and also using a reduced-order model in both nonlinear and linear forms.

Both the experimental and ROM results confirmed that the phenomenon of VIV forever persists even with very high structural damping for an underdamped cylinder (i.e. $\zeta < 1$). Of interest, a simplified linear stability analysis of the ROM (or ROM-LSA) showed that the wake mode in VIV forever was unstable with a constant positive growth rate with increasing reduced velocity. This was distinctly different from the conventional VIV

response of a cylinder with a mass ratio well above the critical value, where the growth rate of the wake mode was negative, leading to vibration amplitude reduction beyond the upper branch.

A further ROM-based analysis of the effect of damping ratio showed that, for an underdamped cylinder (i.e. $\zeta < 1$), the damping ratio has a negligible effect on the vibration amplitude in VIV forever, which is consistent with the experimental results.

On the other hand, both the experimental and ROM results showed that for a sub-critical mass ratio (i.e. $m^* < m_c^*$), the body vibration frequency in the fluid–structure synchronisation region (i.e. the upper branch for $m^* < m_c^*$) tends to increase with damping ratio. Of note, a wavelet-transform-based time–frequency analysis showed that for a cylinder under the critical mass ratio, the vibration frequency is synchronised with the fluid forcing frequency; however, both frequencies appear to be non-stationary over time, suggesting that the frequency synchronisation in VIV forever is associated with chaotic dynamics.

The effect of structural damping on the precise value of the critical mass ratio is to be investigated in future work. It would be of further interest to investigate the nonlinear dynamics (i.e. irregular behaviour with non-stationary frequency components, and chaos) in VIV forever. As implied by the large-amplitude vibration at high structural damping at present, investigation into the energy-harvesting performance from large-amplitude vibration in VIV forever is also warranted.

Funding. This work was supported by the Australian Research Council (J.Z., Discovery Early Career Researcher Award DE200101650; M.C.T., Discovery Project DP190103388; K.H. and M.C.T., Discovery Project DP200100704; and K.H. and J.Z., Discovery Project DP210100990).

Declaration of interests. The authors declare no conflict of interest.

Author ORCIDs.
Peng Han https://orcid.org/0000-0001-6225-969X;
Emmanuel de Langre https://orcid.org/0000-0002-9151-5362;
Mark C. Thompson https://orcid.org/0000-0003-3473-2325;
Kerry Hourigan https://orcid.org/0000-0002-8995-1851;
Jisheng Zhao https://orcid.org/0000-0001-5769-4507.

References

Blevins, R.D. & Coughran, C.S. 2009 Experimental investigation of vortex-induced vibration in one and two dimensions with variable mass, damping, and Reynolds number. *J. Fluids Engng* **131** (10).

Facchinetti, M.L., de Langre, E. & Biolley, F. 2004 Coupling of structure and wake oscillators in vortex-induced vibrations. *J. Fluids Struct.* **19** (2), 123–140.

Govardhan, R. & Williamson, C.H.K. 2000 Modes of vortex formation and frequency response of a freely vibrating cylinder. *J. Fluid Mech.* **420**, 85–130.

Govardhan, R. & Williamson, C.H.K. 2002 Resonance forever: existence of a critical mass and an infinite regime of resonance in vortex-induced vibration. *J. Fluid Mech.* **473**, 147–166.

Grouthier, C., Michelin, S., Modarres-Sadeghi, Y. & de Langre, E. 2013 Self-similar vortex-induced vibrations of a hanging string. *J. Fluid Mech.* **724**.

Han, P., Hémon, P., Pan, G. & de Langre, E. 2021 Nonlinear modeling of combined galloping and vortex-induced vibration of square sections under flow. *Nonlinear Dyn.* **103** (4), 3113–3125.

Han, P. & de Langre, E. 2022 There is no critical mass ratio for galloping of a square cylinder under flow. *J. Fluid Mech.* **931**.

Khalak, A. & Williamson, C.H.K. 1996 Dynamics of a hydroelastic cylinder with very low mass and damping. *J. Fluids Struct.* **10** (5), 455–472.

Konstantinidis, E., Zhao, J., Leontini, J., Lo Jacono, D. & Sheridan, J. 2020 Phase dynamics of effective drag and lift components in vortex-induced vibration at low mass–damping. *J. Fluids Struct.* **96**, 103028.

494 DE LANGRE, E. 2006 Frequency lock-in is caused by coupled-mode flutter. *J. Fluids Struct.* **22** (6-7), 783–791.
495 LEONTINI, J.S., GRIFFITH, M.D., LO JACONO, D. & SHERIDAN, J. 2018 The flow-induced vibration of an
496 elliptical cross-section at varying angles of attack. *J. Fluids Struct.* **78**, 356–373.
497 LEONTINI, J.S., LO JACONO, D. & THOMPSON, M.C. 2011 A numerical study of an inline oscillating
498 cylinder in a free stream. *J. Fluid Mech.* **688**, 551–568.
499 LEONTINI, J.S., LO JACONO, D. & THOMPSON, M.C. 2013 Wake states and frequency selection of a
500 streamwise oscillating cylinder. *J. Fluid Mech.* **730**, 162–192.
501 LIGHTHILL, J. 1986 Fundamentals concerning wave loading on offshore structures. *J. Fluid Mech.* **173**,
502 667–681.
503 LIMACHER, E.J. 2021 Added-mass force on elliptic airfoils. *J. Fluid Mech.* **926**.
504 MOELLER, M.J. 1982 Measurement of unsteady forces on a circular cylinder in cross flow at subcritical
505 Reynolds numbers. Thesis.
506 MORSE, T.L. & WILLIAMSON, C.H.K. 2009 The effect of Reynolds number on the critical mass phenomenon
507 in vortex-induced vibration. *Phys. Fluids* **21** (4), 045105.
508 NAVROSE, & MITTAL, S. 2017 The critical mass phenomenon in vortex-induced vibration at low *Re*. *J. Fluid*
509 *Mech.* **820**, 159–186.
510 NORBERG, C. 2003 Fluctuating lift on a circular cylinder: review and new measurements. *J. Fluids Struct.*
511 **17** (1), 57–96.
512 OGINK, R.H.M. & METRIKINE, A.V. 2010 A wake oscillator with frequency dependent coupling for the
513 modeling of vortex-induced vibration. *J. Sound Vib.* **329** (26), 5452–5473.
514 PAÏDOUSSIS, M.P., PRICE, S.J. & DE LANGRE, E. 2010 *Fluid-Structure Interactions: Cross-Flow-Induced*
515 *Instabilities*. Cambridge University Press.
516 RYAN, K., THOMPSON, M.C. & HOURIGAN, K. 2005 Variation in the critical mass ratio of a freely oscillating
517 cylinder as a function of Reynolds number. *Phys. Fluids* **17** (3), 038106.
518 SHIELS, D., LEONARD, A. & ROSHKO, A. 2001 Flow-induced vibration of a circular cylinder at limiting
519 structural parameters. *J. Fluids Struct.* **15** (1), 3–21.
520 SOTI, A.K., ZHAO, J.S., THOMPSON, M.C., SHERIDAN, J. & BHARDWAJ, R. 2018 Damping effects on
521 vortex-induced vibration of a circular cylinder and implications for power extraction. *J. Fluids Struct.* **81**,
522 289–308.
523 SZEPESSY, S. & BEARMAN, P.W. 1992 Aspect ratio and end plate effects on vortex shedding from a circular
524 cylinder. *J. Fluid Mech.* **234**, 191–217.
525 VIOLETTE, R., DE LANGRE, E. & SZYDLOWSKI, J. 2007 Computation of vortex-induced vibrations of long
526 structures using a wake oscillator model: comparison with dns and experiments. *Comput. Struct.* **85** (11-14),
527 1134–1141.
528 VIOLETTE, R., DE LANGRE, E. & SZYDLOWSKI, J. 2010 A linear stability approach to vortex-induced
529 vibrations and waves. *J. Fluids Struct.* **26** (3), 442–466.
530 WILLIAMSON, C.H.K. & GOVARDHAN, R. 2004 Vortex-induced vibrations. *Annu. Rev. Fluid Mech.* **36** (1),
531 413–455.
532 ZHAO, J., HOURIGAN, K. & THOMPSON, M.C. 2018 Flow-induced vibration of D-section cylinders: an
533 afterbody is not essential for vortex-induced vibration. *J. Fluid Mech.* **851**, 317–343.
534 ZHAO, J., LEONTINI, J.S., LO JACONO, D. & SHERIDAN, J. 2014 Fluid–structure interaction of a square
535 cylinder at different angles of attack. *J. Fluid Mech.* **747**, 688–721.
536 ZHAO, J., THOMPSON, M.C. & HOURIGAN, K. 2022*a* Damping effect on transverse flow-induced vibration
537 of a rotating circular cylinder and its implied energy harvesting performance. *Phys. Rev. Fluids* **7** (2),
538 023905.
539 ZHAO, J., THOMPSON, M.C. & HOURIGAN, K. 2022*b* Decomposition of fluid forcing and phase
540 synchronisation for in-line vortex-induced vibration of a circular cylinder. *J. Fluid Mech.* **941**, R4.